

Signature of the microcavity exciton polariton relaxation mechanism in the polarization of emitted light

Georgios Roumpos,^{1,*} Chih-Wei Lai,^{1,2} T. C. H. Liew,³ Yuri G. Rubo,^{4,5} A. V. Kavokin,^{4,6} and Yoshihisa Yamamoto^{1,2}

¹*E. L. Ginzton Laboratory, Stanford University, Stanford, CA, 94305, USA*

²*National Institute of Informatics, Hitotsubashi, Chiyoda-ku, Tokyo 101-8430, Japan*

³*Centre for Quantum Technologies, National University of Singapore, Singapore 117543*

⁴*School of Physics and Astronomy, University of Southampton, Highfield, Southampton SO17 1BJ, UK*

⁵*Centro de Investigación en Energía, Universidad Nacional Autónoma de México, Temizco, Morelos, 62580, Mexico*

⁶*Marie-Curie Chair of Excellence "Polariton devices", University of Rome II, 1, via della Ricerca Scientifica, Rome, 00133, Italy*

(Dated: November 29, 2018)

We have performed real and momentum space spin-dependent spectroscopy of spontaneously formed exciton polariton condensates for a non-resonant pumping scheme. Under linearly polarized pump, our results can be understood in terms of spin-dependent Boltzmann equations in a two-state model. This suggests that relaxation into the ground state occurs after multiple phonon scattering events and only one polariton-polariton scattering. For the circular pumping case, in which only excitons of one spin are injected, a bottleneck effect is observed, implying inefficient relaxation.

PACS numbers: 78.67.De, 03.75.Nt, 78.70.-g

I. INTRODUCTION

Bose-Einstein condensation (BEC) is an active field of research, especially after its realization in dilute alkali gases^{1,2}. Microcavity exciton polaritons^{3,4,5}, composite quasi-particles consisting of quantum well (QW) exciton and microcavity photon components, have been proposed as candidates for BEC⁶. Due to their low mass, the critical temperature for BEC is expected to be high, even up to room temperature⁷. The confinement in two dimensions, along with the dual exciton-photon character of polaritons, enables interesting optical studies. Indeed, several characteristic signatures of dynamical condensation have been reported in recent years^{8,9,10}.

However, the lifetime of polaritons is short, on the order of 10 psec in our GaAs-based sample when condensation is observed, so the system is inherently dynamical. In previous studies, the final energy distribution of polaritons was compared to the Bose-Einstein distribution for steady-state⁹ or time-resolved¹¹ data. These results are explained by modeling the relaxation mechanism in terms of polariton-acoustic phonon and polariton-polariton scattering^{12,13,14}. However, taking into account the polariton spin degree of freedom introduces further complications, due to the interplay between energy and spin relaxation^{15,16,17}.

Here, we report the insights we gained on the relaxation mechanism, based on polarization-dependent studies of exciton polariton condensation under non-resonant incoherent pumping. For linearly polarized pump, the condensate emission develops both non-zero linear and circular polarization. We observed rotation of the linear polarization axis by $\sim 90^\circ$ between the pump and condensate. The exact rotation angle is correlated with the handedness of the observed circular po-

larization. These signatures are similar to the observations of a parametric oscillator experiment¹⁸, which were interpreted¹⁹ in terms of spin-asymmetric polariton-polariton interaction^{20,21,22}. We use a two-state model employing the spin-dependent Boltzmann equations¹⁶ to understand our experimental results. The agreement we obtain reveals the similarities of the non-resonant pumping scheme to parametric oscillator (magic angle) geometries²³. In the former case, it is believed that polaritons suffer multiple scatterings with phonons and other polaritons before reaching the $k_x \sim 0$ region, so any phase coherence inherited from the laser should be lost, whereas in the latter case only one polariton-polariton interaction occurs²⁴. Further, the observed spectra under circular pumping, show a bottleneck effect. This suggests that polaritons cannot efficiently relax into the ground state when only one spin species is present. A similar suppression of the scattering rate was observed in parametric amplification experiments^{25,26}.

In Section II we describe our experimental setup. Our measurements of the Stokes vector and the corresponding theoretical model are presented in Sections III and IV respectively. Section V covers the relaxation bottleneck under circularly-polarized pumping. Our conclusions are drawn in Section VI. In the Appendix, we write down the equations used in our theoretical model.

II. EXPERIMENTAL SETUP

The sample is the same as in Ref. 27. It consists of an AlAs $\frac{\lambda}{2}$ cavity sandwiched between two distributed Bragg reflector (DBR) mirrors. The upper and lower mirrors are made of 16 and 20 pairs respectively of AlAs and Ga_{0.8}Al_{0.2}As. 3 stacks of 4 GaAs QW's are grown at the central three antinodes of the cavity. The spec-

troscopy setup is described in Ref. 28, and it allows us to perform near field (NF - real space) and far field (FF - momentum space) imaging and spectroscopy. That is, we can measure energy-resolved luminescence as a function of position or of in-plane momentum. The measurements reported here are taken from a spot on the sample with photon-exciton detuning $\delta = +6meV$, while the Rabi splitting is $2\hbar\Omega_{Rabi} = 14meV$. The sample is kept at a temperature of $7 - 8K$ on the cold finger of a He flow cryostat. The system is pumped with a mode-locked Ti-Sapphire laser of 2psec pulse width and 76MHz repetition rate focused on an ellipse of diameters $50\mu m$ and $30\mu m$. For FF data, luminescence is collected through an aperture at the first image plane corresponding to a circular area of $30\mu m$ diameter on the sample. The pumping laser is incident at an angle of 55° (Fig. 1 inset, corresponding wavenumber $k_y = -7\mu m^{-1}$), at the exciton resonance wavelength. The setup employs liquid crystal polarization components as shown in Fig. 1(a). We can pump with linear polarization of varying angle θ_p , as well as general elliptical polarization. The detection can be performed for linear polarization of arbitrary angle θ_d , or for right- and left-circular polarization.

Using the transfer matrix method^{29,30} for exciton inhomogeneous broadening of $3meV$, as measured at the far blue detuned regime, we estimate that the absorbed laser power for TM ($\theta_p = 90^\circ$) and TE ($\theta_p = 0^\circ$) pumping is $\sim 4\%$ and $\sim 0.9\%$ respectively of the incident power. We assume that the absorption efficiency is independent of power. In the rest of the paper, the various pump polarization states refer to the actually absorbed light inside the cavity, taking into account the calculated differential absorption of TM and TE pumping.

A ground state ($k_{x,y} = 0$) linear polarization splitting of $\sim 50\mu eV$, similar to earlier studies^{18,31,32}, is measured for low excitation power and the current sample orientation, (Fig. 1(b-c)) possibly due to crystal asymmetry or strain. The observed superimposed linear polarization splitting for $k_x \neq 0$ is in quantitative agreement with a transfer matrix calculation (Fig. 1(b) inset).

III. STOKES VECTOR MEASUREMENT

The polarization state of light is characterized by the following three parameters (normalized with respect to the total power), which are equivalent to the Stokes parameters as originally defined³³:

$$S_1 = \frac{I_{0^\circ} - I_{90^\circ}}{I_{0^\circ} + I_{90^\circ}}, \quad S_2 = \frac{I_{45^\circ} - I_{-45^\circ}}{I_{45^\circ} + I_{-45^\circ}}, \quad S_3 = \frac{I_L - I_R}{I_L + I_R}. \quad (1)$$

I_{0° , I_{90° , I_{45° , and I_{-45° are the intensities of the linearly polarized components at $\theta_d = 0^\circ$, 90° , 45° , and -45° respectively. I_L and I_R are the intensities of the left- and right-circularly polarized components respectively. From the above parameters, we can calculate the degree of linear polarization (DOLP) and the angle of the major lin-

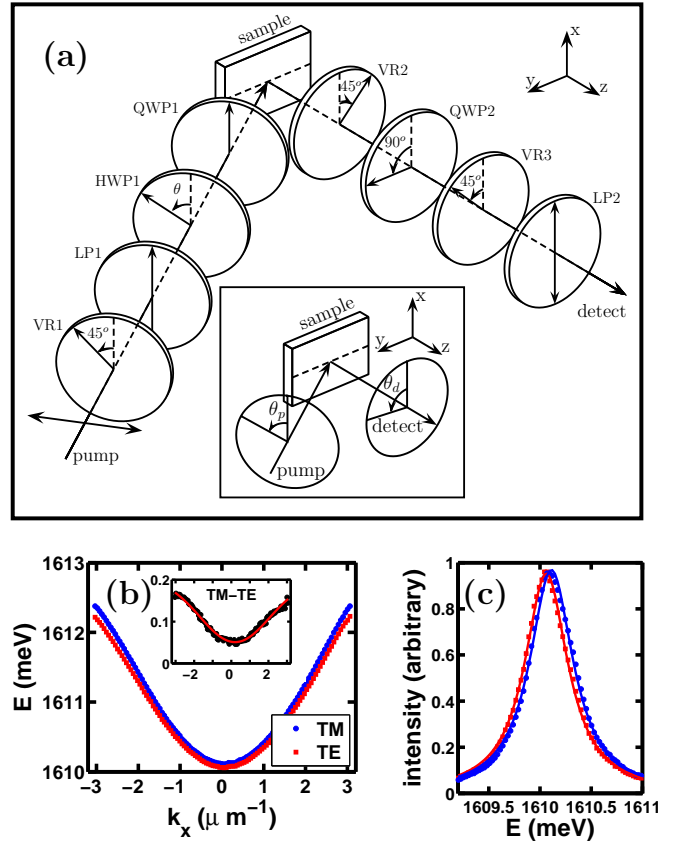


FIG. 1: (color online) (a) The polarization measurement setup. Vectors label the fast or polarization axes of the optical components. The laser pump is initially horizontally polarized ($\theta_p = 90^\circ$), and is incident at an angle of 55° with respect to the growth direction z . Luminescence is collected along the z -axis. The first variable retarder (VR1) and linear polarizer (LP1) work as a variable attenuator. By rotating a half waveplate (HWP1), and by using a removable quarter waveplate (QWP1), we can implement various polarization states for the pump. The second variable retarder (VR2) is used as a zero, half, or quarter waveplate. The combination of a quarter waveplate (QWP2), variable retarder (VR3) and linear polarizer (LP2) is used for detection of a particular linear polarization state, depending on the retardance of VR3. Inset: Definition of angles θ_p and θ_d corresponding to the polarization axes of the pump and detection respectively. (b) Measured dispersion curves for TM ($\theta_d = 0^\circ$ - blue dots) and TE ($\theta_d = 90^\circ$ - red squares) luminescence for low excitation density ($60\mu m^{-2}$ per pulse per QW). The plotted points are the first moments of measured spectra for every k_x . A small ground state splitting is visible. $k_x = 3\mu m^{-1}$ corresponds to 21° in air. Inset: The measured TM-TE splitting (black dots) and the theoretical prediction for our sample parameters with a superimposed ground state splitting of $50\mu eV$ (red line). (c) Measured spectra for $k_x = 0$ (points) fitted with Lorentzians (lines).

ear polarization axis ψ

$$DOLP = \sqrt{S_1^2 + S_2^2}, \quad \psi = \frac{1}{2} \arctan\left(\frac{S_2}{S_1}\right). \quad (2)$$

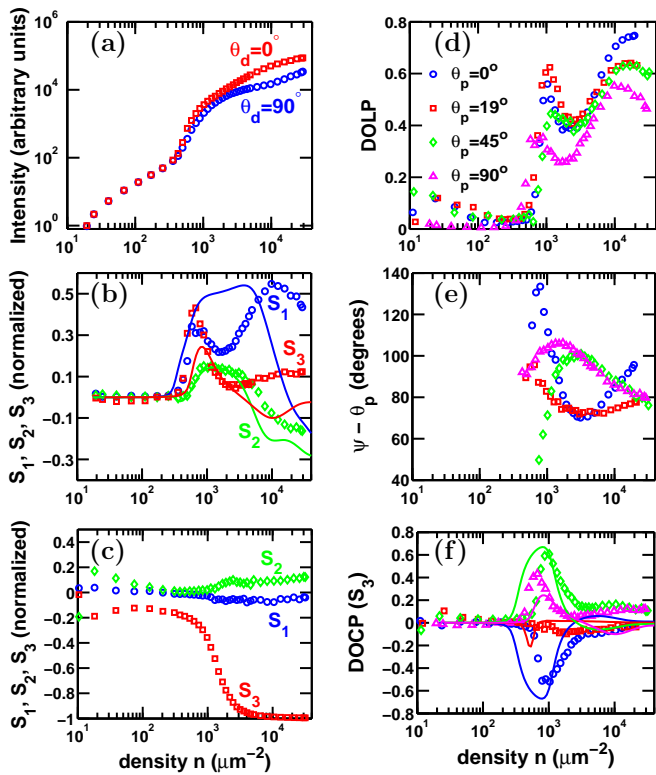


FIG. 2: (color online) Measurement of Stokes parameters (markers) compared with the theoretical model (solid lines). (a) Horizontal pumping ($\theta_p = 90^\circ$). Collected luminescence for $\theta_d = 0^\circ$ (red squares) and $\theta_d = 90^\circ$ (blue circles) vs. injected particle density in μm^{-2} per pulse per QW. A clear threshold is observed at $5 \times 10^2 \mu\text{m}^{-2}$. (b-c) Degree of polarization measurement for (b) $\theta_p = 90^\circ$ linear pumping and (c) left circularly polarized pumping. Blue circles: S_1 , green diamonds: S_2 , red squares: S_3 defined in eq. (1). (d-f) Calculated polarization parameters from the measurement of the Stokes parameters for linear pumping (eqs. (1-2)). (d) DOLP. (e) Angle for major axis of linear polarization ψ relative to θ_p . (f) Degree of circular polarization (S_3).

We record the far field spectra for varying pumping power and polarization angles θ_p and θ_d , and sum the intensities inside the area $|k_x| < 0.55 \mu\text{m}^{-1}$ (corresponding to 4°). The observed normalized intensities I_{θ_d} are only weakly dependent on the choice of this area, and are shown in Fig. 2. In Fig. 2(a) we plot the measured luminescence intensity for linearly polarized light along $\theta_d = 0^\circ$ and $\theta_d = 90^\circ$ as a function of pumping power in units of the generated polariton density per pulse per QW. The pump is horizontally polarized ($\theta_p = 90^\circ$). The data show a non-linear increase above a threshold density of $\sim 400 \mu\text{m}^{-2}$, which marks the onset of condensation. By measuring all six intensities required by equation (1), we calculate the three Stokes parameters. The results for this pump polarization ($\theta_p = 90^\circ$) are plotted in Fig. 2(b) along with the theoretical curves, to be discussed in the next section.

For circularly polarized pump (Fig. 2(c)) and well

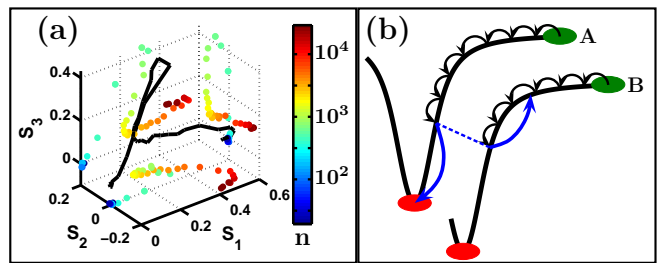


FIG. 3: (color online) (a) The path followed by the polarization vector for increasing excitation power ($\theta_p = 90^\circ$ linearly polarized pumping). The projections on the three normal planes are shown with colored dots, the color scale corresponding to the injected polariton density n in μm^{-2} per pulse per quantum well (QW), as shown in the colorbar. (b) Schematic of the proposed relaxation mechanism: the optically excited polariton A, first loses energy by phonon scattering, then scatters with one other polariton (B) and populates the ground state.

above threshold, the signal is perfectly circularly polarized, up to -99.4% . This is due to the short polariton lifetime ($\sim 10\text{ps}$), which is shorter than the spin relaxation time. The negative sign of S_3 means that the angular momentum of the emitted photons along the z-axis is the same as that of the optically injected exciton polaritons, since we pump and detect from the same side of the sample (Fig. 1(a)).

We next focus on linearly polarized pumping and vary the direction of linear polarization for the pump (θ_p). Above threshold, a non-zero degree of linear polarization develops (Fig. 2(d)), while the polarization direction is rotated by $\sim 90^\circ$ compared to the pump (Fig. 2(e)). Also, a circularly polarized component emerges, with S_3 changing sign for varying θ_p (Fig. 2(f)). The sign change is correlated with the deviation of $\psi - \theta_p$ from 90° . The path followed by the polarization vector for increasing power and $\theta_p = 90^\circ$ linearly polarized pumping is plotted in Fig. 3(a).

IV. THEORETICAL MODEL

To interpret these results we have used a simplified model based on the spin-dependent Boltzmann equations for polaritons in microcavities¹⁶. Our model is based upon two states, representing the condensate and reservoir, each characterized by a 2×2 spin density matrix. The polariton-polariton scattering matrix element in parallel spin configuration, α_1 (positive), is believed to be much greater in magnitude^{19,21} than that in antiparallel configuration, α_2 (negative). Therefore, calculating the transition rates we keep only terms $\propto \alpha_1^2$ and the interference terms $\propto \alpha_1\alpha_2$. We assume the reservoir is quickly populated by the pump from fast polariton-phonon relaxation. Then we consider the polariton-polariton scattering processes, which populate the condensate (Fig. 3(b)).

The spin-anisotropy of the polariton-polariton interactions gives rise to two important effects. First, a 90° rotation of the linear polarization appears upon one polariton-polariton scattering, which has been evidenced in parametric oscillator experiments in magic angle¹⁸ as well as degenerate configurations³⁴. This is because of the difference between the scattering matrix elements of linearly polarized polaritons

$$\langle \phi, \phi | V | \phi, \phi \rangle = \frac{1}{2} (\alpha_1 + \alpha_2), \quad (3)$$

$$\langle \phi + 90^\circ, \phi + 90^\circ | V | \phi, \phi \rangle = \frac{1}{2} (\alpha_1 - \alpha_2). \quad (4)$$

V is the polariton-polariton interaction operator, and $|\phi\rangle$ is the linear superposition $\frac{1}{\sqrt{2}} (|\uparrow\rangle + e^{2i\phi} |\downarrow\rangle)$ of spin-up and spin-down polaritons. We note that if multiple polariton-polariton scattering events are involved, the initial polarization information should be lost.

Second, if there is an imbalance of the populations in the two spin components (in either the condensate or the reservoir) then a self-induced Larmor precession of the condensate and reservoir Stokes vector occurs. This is because of the difference in the polariton-polariton interaction energy between the different spin components. This precession becomes faster by increasing the polariton population. Therefore, at high pumping rates, the degree of linear polarization of the luminescence decays in our time-integrated data (Fig. 2(d)).

Other polarization sensitivity derives from an assumed energy splitting between states linearly polarized at 19° and 109° , as is evidenced from Fig. 1(c) and from the lack of circularly polarized component in the luminescence for excitation with $\theta_p = 19^\circ$. This splitting causes a rotation of the Stokes vector if the reservoir state is not an eigenstate with linear polarization of 19° or 109° , which results in non-zero S_3 (Fig. 2(f)). The condensate Stokes parameters are time integrated and normalized by the time integrated condensate population for comparison to the experimental results.

The results of our model are represented by solid lines in Fig. 2. We assumed a condensate lifetime of $2ps$, reservoir lifetime of $100ps$, pulse duration of $2ps$, $\alpha_2/\alpha_1 = -0.025$, and polarization splittings of $50\mu eV$ for both the condensate and reservoir. The final equations and the value we used for α_1 are provided in the Appendix. The main features of our experimental results are explained within this model.

V. RELAXATION BOTTLENECK UNDER CIRCULARLY-POLARIZED PUMPING

In Fig. 4 we compare the FF and NF spectra for two pumping schemes, namely linear ($\theta_p = 90^\circ$, Fig. 4(a-b)) and left-circular (Fig. 4(c-d)) polarizations. Under linear pumping, we observe that the linewidth narrows at threshold, and luminescence is concentrated around $k_x = 0$ and $x = 0$. For higher excitation power, the

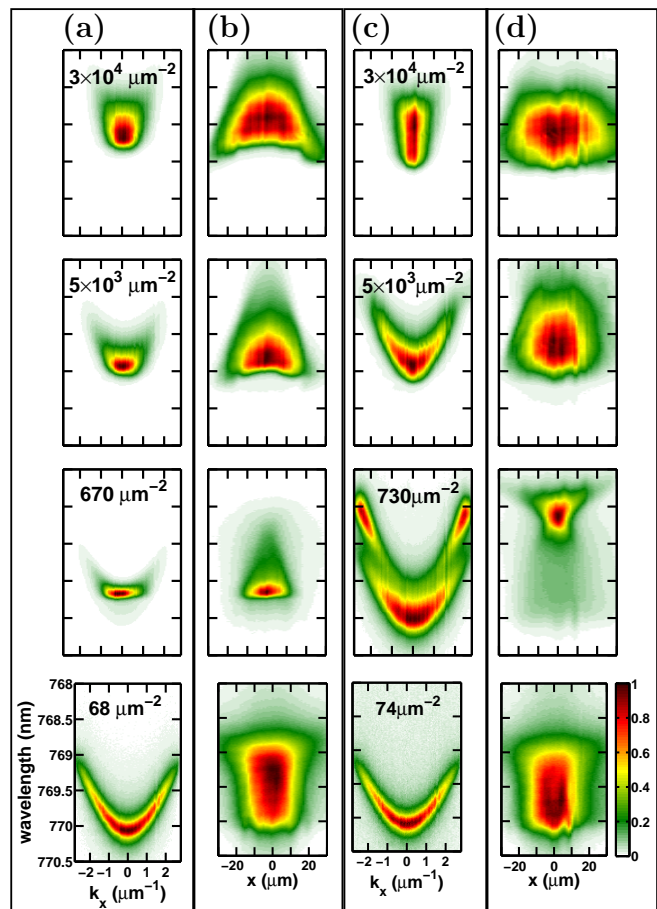


FIG. 4: (color online) Far-field (FF) (k_x in μm^{-1} vs. wavelength in nm) and near-field (NF) (x in μm vs. wavelength in nm) spectra for various injected particle densities (in μm^{-2} per pulse per QW). (a) FF, $\theta_p = 90^\circ$, $\theta_d = 0^\circ$. (b) NF, same pumping-detection scheme. (c) FF, left circular pump, right circular detection. Note that the projection of angular momentum along the z -axis (Fig. 1(a)) has the same sign for both pump and detected photons. (d) NF, same pumping-detection scheme.

momentum and position distributions broaden and the condensate energy blue-shifts. Under circular pumping and at just above threshold, relaxation bottleneck is observed in momentum space at $k_x \sim \pm 2.3\mu m^{-1}$ ($\pm 16^\circ$ in air), while in real space luminescence is concentrated at the center of the excitation spot. This implies that relaxation into the zero momentum region is only efficient when both spin species are present. For higher excitation power, luminescence is mainly observed around $k_x = 0$ and $x = 0$, similar to the linear pumping case. This result is consistent with previous parametric amplification experiments^{25,26}, where a suppression of the scattering rate towards the zero-momentum region was observed when only one spin species was present.

Polariton condensation is a competition between relaxation and decay from the cavity. Our data suggest that relaxation is more efficient in the linearly polarized pump

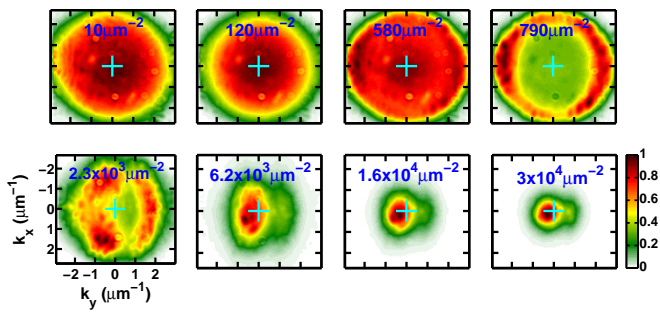


FIG. 5: (color online) Momentum space images for left-circularly polarized pumping and right-circularly polarized detection (same scheme as in Fig. 4(c-d)). For increasing pumping power, a ring pattern develops and the images lose reflection symmetry. The cyan crosses mark the origin in each figure. The pump is incident at $(k_x, k_y) = (0, -7)\mu\text{m}^{-1}$.

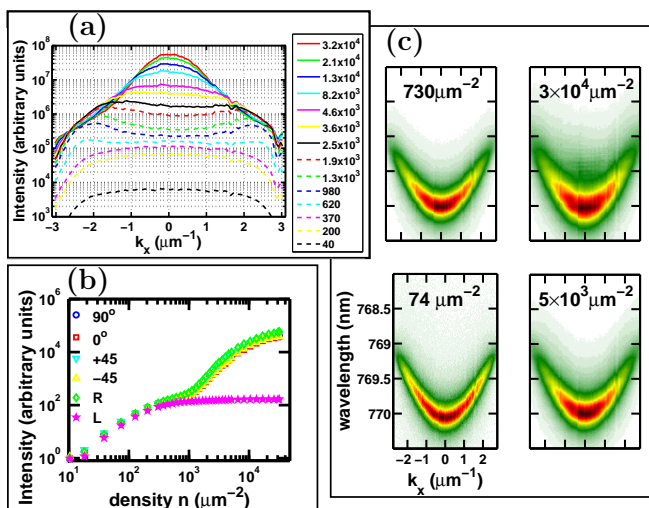


FIG. 6: (color online) (a) The momentum space distribution along the x-axis for various polariton densities n (in μm^{-2} per pulse per QW). The pump is left-circularly polarized, and the detection right-circularly polarized (same scheme as in Figs. 4(c-d) and 5). At $n \sim 600\mu\text{m}^{-2}$ two peaks appear around $k_x = \pm 2.3\mu\text{m}^{-1}$, which move towards $k_x = 0\mu\text{m}^{-1}$ for increasing n . Eventually, a central peak appears and dominates the luminescence. (b) Luminescence inside the area $|k_x| < 0.55\mu\text{m}^{-1}$ for the six different polarization states of eq. 1 as a function of polariton density under left-circularly polarized pumping. A stimulation threshold is observed at $n \sim 10^3\mu\text{m}^{-2}$. (c) Far-field (FF) spectra for left-circularly polarized detection (represented by magenta stars in (b)) for various pumping powers. A broad distribution following the lower polariton dispersion is always observed.

case, whereas decay is more efficient in the circularly polarized pump case. On the other hand, our simple two-state model treats the relaxation rate as a free parameter. Derivation of this rate involves a full many-body calculation, where all states in momentum space need to be considered. A more sophisticated model is therefore needed to understand the results of this section.

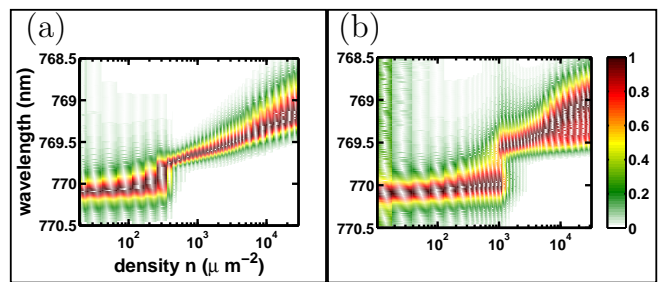


FIG. 7: (color online) (a) The measured spectra near zero momentum ($|k_x| < 0.55\mu\text{m}^{-1}$) for linearly polarized pumping ($\theta_p = 90^\circ$, $\theta_d = 0^\circ$) as a function of polariton density. (b) Same spectra for left-circularly polarized pump and right-circularly polarized detection.

The inefficient cooling for the circular pumping case is further evidenced in the FF images presented in Fig. 5 for various pumping powers. Above threshold, they do not possess the $k_y \leftrightarrow -k_y$ reflection symmetry. The laser pump is incident at $(k_x, k_y) = (0, -7)\mu\text{m}^{-1}$, so the polariton distribution is shifted towards the source. On the contrary, under linearly polarized pumping the momentum space distribution is always spherically symmetric. Detailed data of the momentum space distribution along the x -axis for increasing pumping power are shown in Fig. 6(a). The cross-circularly polarized component is much weaker above a threshold pumping power, as shown in Fig. 6(b), and does not condense (Fig. 6(c)).

Fig. 7(a) shows the measured spectra near zero momentum ($|k_x| < 0.55\mu\text{m}^{-1}$) for linearly polarized pumping ($\theta_p = 90^\circ$, $\theta_d = 0^\circ$). We observe a linewidth decrease and blue shift just above threshold. We note that the observed energy shift shows an almost logarithmic increase as a function of pumping power, similar to Ref. 35. From a polariton-polariton interaction point of view, a linear increase would be expected. Fig. 7(b) shows the same spectra for left-circularly polarized pump and right-circularly polarized detection. We observe a similar blue shift, but no linewidth narrowing. The reason for the different spectral linewidths is not well understood. It might indicate that the temporal coherence is not necessarily enhanced with increasing accumulation of polaritons near the zero in-plane momentum.

VI. CONCLUSIONS

In conclusion, we studied polarization-dependent luminescence from an exciton polariton system as a function of pump power and polarization in a non-resonant pumping geometry. Spin-dependent polariton-polariton interaction manifests itself in the rotation of the linear polarization axis by $\sim 90^\circ$ under linearly polarized pumping. This can be understood in terms of a two-state model, suggesting that polaritons populate the condensate after multiple phonon scatterings and only one polariton-

polariton scattering. In addition, when only one spin species is injected, we observed a relaxation bottleneck. This phenomenon is typically attributed to inefficient relaxation, leading to photon leakage from the cavity before polaritons reach the zero-momentum region. Full determination of the polarization of polariton condensates reveals that the spin degree of freedom plays an important role in understanding the relaxation mechanism of microcavity exciton polaritons.

Acknowledgments

G.R. acknowledges support from JST/SORST and Special Coordination Funds for Promoting Science and Technology. T.C.H.L., Y.G.R., and A.V.K. would like to thank E.P.S.R.C. for financial support. A.V.K. thanks Ivan Shelykh for useful comments.

APPENDIX

Here we present the equations used in the theoretical model of Section IV. The approach we have taken is based on the spin-dependent Boltzmann equations for exciton-polaritons in microcavities of Ref. 16. We have considered two states, reservoir and condensate, each characterised by a 2×2 spin density matrix

$$\begin{bmatrix} R_{\uparrow} & (R_x - iR_y) \\ (R_x + iR_y) & R_{\downarrow} \end{bmatrix}, \quad \begin{bmatrix} N_{\uparrow} & (S_x - iS_y) \\ (S_x + iS_y) & N_{\downarrow} \end{bmatrix}. \quad (\text{A.1})$$

Here R_{\uparrow} and R_{\downarrow} are the reservoir populations for spin-up and spin-down polaritons, R_x and R_y are the pseudospin components that characterize the linear polarization degree measured in the horizontal-vertical and diagonal basis, respectively. The circularly polarized component R_z of reservoir pseudospin is $R_z = (R_{\uparrow} - R_{\downarrow})/2$. The corresponding numbers for the condensate are given by N_{\uparrow} , N_{\downarrow} , S_x , S_y , and $S_z = (N_{\uparrow} - N_{\downarrow})/2$. P_{\uparrow} , P_{\downarrow} , P_x , and P_y describe the pump. For example, for TE pumping ($\theta_p = 0^\circ$), we have $P_{\uparrow} = P_{\downarrow} = P_x$. The full rate equations we used are as follows,

$$\frac{dN_{\uparrow}}{dt} = -\Gamma N_{\uparrow} + (\omega_x S_y - \omega_y S_x) + W R_{\uparrow}^2 (N_{\uparrow} + 1), (\text{A.2})$$

$$\frac{dN_{\downarrow}}{dt} = -\Gamma N_{\downarrow} - (\omega_x S_y - \omega_y S_x) + W R_{\downarrow}^2 (N_{\downarrow} + 1), (\text{A.3})$$

$$\begin{aligned} \frac{dS_x}{dt} = & -\Gamma S_x + \omega_y S_z - \frac{(\alpha_1 - \alpha_2)}{\hbar} (S_z + R_z) S_y \\ & + \frac{W}{2} (R_{\uparrow}^2 + R_{\downarrow}^2) S_x \\ & + \frac{W}{2} \frac{\alpha_2}{\alpha_1} (R_{\uparrow} + R_{\downarrow}) (N_{\uparrow} + N_{\downarrow} + 2) R_x (\text{A.4}) \end{aligned}$$

$$\begin{aligned} \frac{dS_y}{dt} = & -\Gamma S_y - \omega_x S_z + \frac{(\alpha_1 - \alpha_2)}{\hbar} (S_z + R_z) S_x \\ & + \frac{W}{2} (R_{\uparrow}^2 + R_{\downarrow}^2) S_y \\ & + \frac{W}{2} \frac{\alpha_2}{\alpha_1} (R_{\uparrow} + R_{\downarrow}) (N_{\uparrow} + N_{\downarrow} + 2) R_y, (\text{A.5}) \end{aligned}$$

$$\begin{aligned} \frac{dR_{\uparrow}}{dt} = & -\gamma R_{\uparrow} + (\Omega_x R_y - \Omega_y R_x) - W R_{\uparrow}^2 (N_{\uparrow} + 1) \\ & + P_{\uparrow}, (\text{A.6}) \end{aligned}$$

$$\begin{aligned} \frac{dR_{\downarrow}}{dt} = & -\gamma R_{\downarrow} - (\Omega_x R_y - \Omega_y R_x) - W R_{\downarrow}^2 (N_{\downarrow} + 1) \\ & + P_{\downarrow}, (\text{A.7}) \end{aligned}$$

$$\begin{aligned} \frac{dR_x}{dt} = & -\gamma R_x + \Omega_y R_z - \frac{(\alpha_1 - \alpha_2)}{\hbar} (S_z + R_z) R_y \\ & - \frac{W}{2} [(N_{\uparrow} + 1) R_{\uparrow} + (N_{\downarrow} + 1) R_{\downarrow}] R_x + P_x, (\text{A.8}) \end{aligned}$$

$$\begin{aligned} \frac{dR_y}{dt} = & -\gamma R_y - \Omega_x R_z + \frac{(\alpha_1 - \alpha_2)}{\hbar} (S_z + R_z) R_x \\ & - \frac{W}{2} [(N_{\uparrow} + 1) R_{\uparrow} + (N_{\downarrow} + 1) R_{\downarrow}] R_y + P_y (\text{A.9}) \end{aligned}$$

Here $\omega_{x,y}$ and $\Omega_{x,y}$ are the Larmor frequencies corresponding to the effective magnetic field due to the polarization splitting. $\omega_{x,y}$ refer to the condensate and $\Omega_{x,y}$ refer to the reservoir. Γ and γ are the decay rates for the condensate and reservoir, respectively. As discussed in Section IV, we use the values

$$\begin{aligned} \omega_x = \Omega_x = & \frac{50 \mu\text{eV}}{\hbar} \cos(2 \times 19^\circ), \\ \omega_y = \Omega_y = & \frac{50 \mu\text{eV}}{\hbar} \sin(2 \times 19^\circ), \\ \Gamma = 0.5 \text{ ps}^{-1}, \quad \gamma = & 0.01 \text{ ps}^{-1}. \quad (\text{A.10}) \end{aligned}$$

The scattering rate from the reservoir to condensate is $W = (2\pi/\hbar)\alpha_1^2 \rho_i$, where ρ_i is the density of polariton states at the idler energy. The idler energy is $E_i = 2E_r - E_c$, where E_r and E_c are the energies of polaritons in the reservoir and condensate, respectively.

We have used the value of $\alpha_1 = 5 \times 10^{-4}$ meV, which is the estimate of the interaction energy of two polaritons inside the excitation spot of $10 \mu\text{m}$ radius. The scattering rate is estimated as $W = 5 \times 10^{-7}$ ps $^{-1}$.

- * Electronic address: roumpos@stanford.edu
- ¹ M. H. Anderson, J. R. Ensher, M. R. Matthews, C. E. Wieman, and E. A. Cornell, *Science* **269**, 198 (1995).
 - ² K. B. Davis, M. O. Mewes, M. R. Andrews, N. J. van Druten, D. S. Durfee, D. M. Kurn, and W. Ketterle, *Phys. Rev. Lett.* **75**, 3969 (1995).
 - ³ C. Weisbuch, M. Nishioka, A. Ishikawa, and Y. Arakawa, *Phys. Rev. Lett.* **69**, 3314 (1992).
 - ⁴ Y. Yamamoto, F. Tassone, and H. Cao, *Semiconductor Cavity Quantum Electrodynamics* (Springer-Verlag, 2000).
 - ⁵ A. Kavokin and G. Malpuech, *Cavity Polaritons* (Academic Press, 2003).
 - ⁶ A. Imamoglu, R. J. Ram, S. Pau, and Y. Yamamoto, *Phys. Rev. A* **53**, 4250 (1996).
 - ⁷ S. Christopoulos, G. B. H. von Högersthal, A. J. D. Grundy, P. G. Lagoudakis, A. V. Kavokin, J. J. Baumberg, G. Christmann, R. Butté, E. Feltn, J.-F. Carlin, et al., *Phys. Rev. Lett.* **98**, 126405 (2007).
 - ⁸ H. Deng, G. Weihs, D. Snoke, J. Bloch, and Y. Yamamoto, *Proc. Natl. Acad. Sci. U.S.A.* **100**, 15318 (2003).
 - ⁹ J. Kasprzak, M. Richard, S. Kundermann, A. Baasand, P. Jeambrun, J. M. J. Keeling, F. M. Marchetti, M. H. Szymańska, R. André, J. L. Staehli, et al., *Nature* **443**, 409 (2006).
 - ¹⁰ H. Deng, G. S. Solomon, R. Hey, K. H. Ploog, and Y. Yamamoto, *Phys. Rev. Lett.* **99**, 126403 (2007).
 - ¹¹ H. Deng, D. Press, S. Gotzinger, G. S. Solomon, R. Hey, K. H. Ploog, and Y. Yamamoto, *Phys. Rev. Lett.* **97**, 146402 (2006).
 - ¹² F. Tassone and Y. Yamamoto, *Phys. Rev. B* **59**, 10830 (1999).
 - ¹³ D. Porras, C. Ciuti, J. J. Baumberg, and C. Tejedor, *Phys. Rev. B* **66**, 085304 (2002).
 - ¹⁴ T. D. Doan, H. T. Cao, D. B. T. Thoai, and H. Haug, *Phys. Rev. B* **72**, 085301 (2005).
 - ¹⁵ K. V. Kavokin, I. A. Shelykh, A. V. Kavokin, G. Malpuech, and P. Bigenwald, *Phys. Rev. Lett.* **92**, 017401 (2004).
 - ¹⁶ I. A. Shelykh, A. V. Kavokin, and G. Malpuech, *Phys. Stat. Solidi. b* **242**, 2271 (2005).
 - ¹⁷ H. T. Cao, T. D. Doan, D. B. T. Thoai, and H. Haug, *Phys. Rev. B* **77**, 075320 (2008).
 - ¹⁸ D. N. Krizhanovskii, D. Sanvitto, I. A. Shelykh, M. M. Glazov, G. Malpuech, D. D. Solnyshkov, A. Kavokin, S. Ceccarelli, M. S. Skolnick, and J. S. Roberts, *Phys. Rev. B* **73**, 073303 (2006).
 - ¹⁹ S. Schumacher, N. H. Kwong, and R. Binder, *Phys. Rev. B* **76**, 245324 (2007).
 - ²⁰ M. Kuwata-Gonokami, S. Inouye, H. Suzuura, M. Shirane, R. Shimano, T. Someya, and H. Sakaki, *Phys. Rev. Lett.* **79**, 1341 (1997).
 - ²¹ C. Ciuti, V. Savona, C. Piermarocchi, A. Quattropani, and P. Schwendimann, *Phys. Rev. B* **58**, 7926 (1998).
 - ²² P. R. Eastham and D. M. Whittaker, *Phys. Rev. B* **68**, 075324 (2003).
 - ²³ R. M. Stevenson, V. N. Astratov, M. S. Skolnick, D. M. Whittaker, M. Emam-Ismael, A. I. Tartakovskii, P. G. Savvidis, J. J. Baumberg, and J. S. Roberts, *Phys. Rev. Lett.* **85**, 3680 (2000).
 - ²⁴ J. Keeling, F. M. Marchetti, M. H. Szymańska, and P. B. Littlewood, *Semicond. Sci. Technol.* **22**, R1 (2007).
 - ²⁵ A. I. Tartakovskii, D. N. Krizhanovskii, and V. D. Kulakovskii, *Phys. Rev. B* **62**, R13298 (2000).
 - ²⁶ A. Kavokin, P. G. Lagoudakis, G. Malpuech, and J. J. Baumberg, *Phys. Rev. B* **67**, 195321 (2003).
 - ²⁷ S. Utsunomiya, L. Tian, G. Roumpos, C. W. Lai, N. Kumada, T. Fujisawa, M. Kuwata-Gonokami, A. Lffler, S. Hfling, A. Forchel, et al., *Nature Physics* **4**, 700 (2008).
 - ²⁸ C. W. Lai, N. Y. Kim, S. Utsunomiya, G. Roumpos, H. Deng, M. D. Fraser, T. Byrnes, P. Recher, N. Kumada, T. Fujisawa, et al., *Nature* **450**, 529 (2007).
 - ²⁹ P. Yeh, *Optical Waves in Layered Media* (John Wiley, Hoboken, 2005).
 - ³⁰ Y. Zhu, D. J. Gauthier, S. E. Morin, Q. Wu, H. J. Carmichael, and T. W. Mossberg, *Phys. Rev. Lett.* **64**, 2499 (1990).
 - ³¹ Ł. Kłopotowski, M. D. Martín, A. Amo, L. Viña, I. A. Shelykh, M. M. Glazov, G. Malpuech, A. V. Kavokin, and R. André, *Solid State Commun.* **139**, 511 (2006).
 - ³² J. Kasprzak, R. André, L. S. Dang, I. A. Shelykh, A. V. Kavokin, Y. G. Rubo, K. V. Kavokin, and G. Malpuech, *Phys. Rev. B* **75**, 045326 (2007).
 - ³³ E. Hecht, *Am. J. Phys.* **38**, 1156 (1970).
 - ³⁴ C. Leyder, T. C. H. Liew, A. V. Kavokin, I. A. Shelykh, M. Romanelli, J. P. Karr, E. Giacobino, and A. Bramati, *Phys. Rev. Lett.* **99**, 196402 (2007).
 - ³⁵ D. Bajoni, P. Senellart, E. Wertz, I. Sagnes, A. Miard, A. Lemaître, and J. Bloch, *Phys. Rev. Lett.* **100**, 047401 (2008).